



# Sub-unit cell engineering of CrVO<sub>3</sub> superlattice thin films



Claudio Bellani<sup>1,9</sup>✉, Simon Mellaerts<sup>2,3,9</sup>, Wei-Fan Hsu<sup>2</sup>, Koen Schouteden<sup>2</sup>, Alberto Binetti<sup>2</sup>, Arno Annys<sup>4</sup>, Zezhong Zhang<sup>4</sup>, Nicolas Gauquelin<sup>4</sup>, Johan Verbeeck<sup>4</sup>, Jesús López-Sánchez<sup>5</sup>, Adolfo del Campo<sup>5</sup>, Soon-Gil Jung<sup>6</sup>, Tuson Park<sup>7</sup>, Michel Houssa<sup>2,8</sup>, Jean-Pierre Locquet<sup>2</sup> & Jin Won Seo<sup>1</sup>✉

Ordered corundum oxides introduce new prospects in the field of functional oxides thin films, complementing the more widely studied class of ABO<sub>3</sub> perovskites. In this work, we take advantage of the layer-by-layer growth regime to fabricate epitaxial CrVO<sub>3</sub> superlattice thin films with atomic-scale accuracy on the periodic arrangement of chromium and vanadium layers. By means of X-ray diffraction, scanning transmission electron microscopy and Raman spectroscopy, we confirm the thickness control in the sub-unit cell scale, alternating 3, 2 or 1 single atomic layers of Cr<sub>2</sub>O<sub>3</sub> and V<sub>2</sub>O<sub>3</sub>. We stabilize the ilmenite phase of CrVO<sub>3</sub> (space group R $\bar{3}$ ) and compare the functional properties of the thin film with those calculated by density functional theory. This approach to the growth of ordered corundum oxides opens the path towards the stabilization of complex oxides with tailored properties by varying the composition and the superlattice period, ultimately broadening the family of functional rhombohedral oxides.

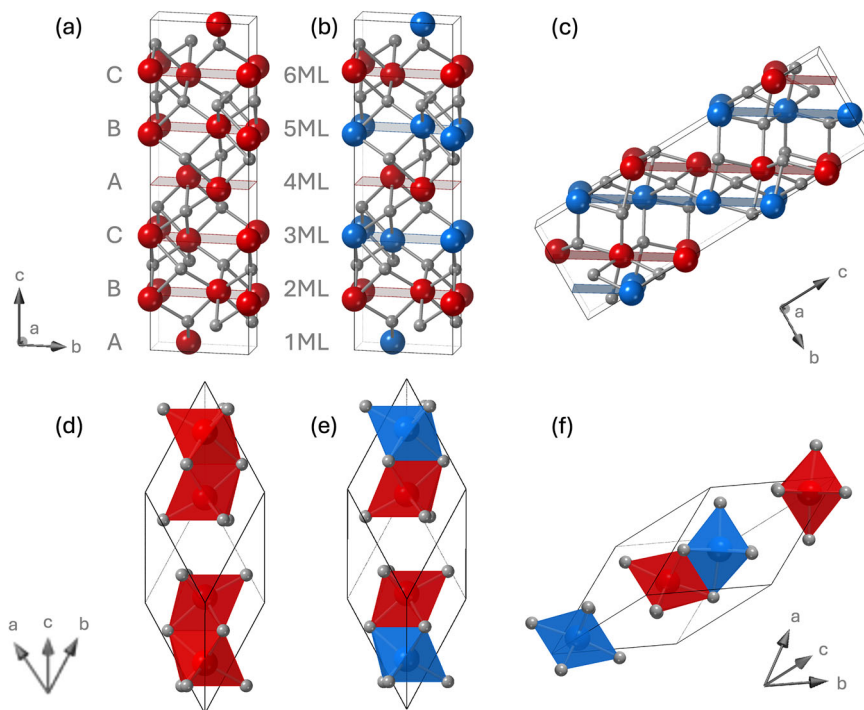
The field of complex oxides has been largely dominated by perovskite oxides, which are among the most extensively studied ABO<sub>3</sub> phases. Their widespread interest stems from their diverse functional properties, including ferroelectricity, colossal magnetoresistance, multiferroicity, and metal-insulator transitions (MITs). This versatility arises from their inherent instability to energy-lowering structural distortions, ultimately governed by the imbalance of ionic radii at the A and B sites, which is quantified by the Goldschmidt tolerance factor<sup>1,2</sup>. In nearly half of all perovskites, this instability manifests as an antiferrodistortive octahedral rotation pattern,  $a^-a^-c^+$ , resulting in an orthorhombic phase with space group Pbnm<sup>3,4</sup>. Interestingly, hexagonal oxides exhibit similar tolerance factors and often compete with orthorhombic polymorphs, as for example in the nickelates<sup>5</sup>. However, when the ionic radii of the A and B cations become more comparable, i.e.,  $r_{\text{ionic}}(\text{A}) \approx r_{\text{ionic}}(\text{B})$ , the system transitions towards the regime of ordered corundum compounds<sup>6</sup>. This parent crystal structure is illustrated in Fig. 1a, d with the R $\bar{3}c$  space group, of which Al<sub>2</sub>O<sub>3</sub>, Cr<sub>2</sub>O<sub>3</sub> and V<sub>2</sub>O<sub>3</sub> are most prominent examples. By defining A and B to be non-equivalent and ordered in the unit cell, the R $\bar{3}$  ilmenite and polar R $\bar{3}c$  lithium niobate (LNO) symmetries can be established, as shown in Fig. 1b, c, respectively.

These layered corundum compounds differ both structurally and chemically from the class of perovskites. Their small tolerance factor carries profound implications. First, they exhibit a high crystal density, where both A and B cations reside in equivalent octahedral environments. Second, the presence of face-sharing octahedra results in extremely short A–B distances, facilitating direct metal–metal bonding-distinct from the hybridization of oxygen atoms in A–O–B bonds found in perovskite materials. Lastly, the A and B sites can be occupied by similar transition metals, giving rise to strong electron correlations and associated phenomena, such as superconductivity and MITs<sup>7</sup>.

In light of these considerations, the stabilization of new ordered corundum thin films offers intriguing opportunities in the field of functional oxides. On the one hand, the combination of two magnetic sublattices with strong electron correlations can lead to MITs; on the other hand, new multiferroic compounds can be stabilized if ordered in the polar space group R $\bar{3}c$ <sup>8,9</sup>. All together, polar metals with magnetoelectric coupling can be targeted<sup>10,11</sup>. To date, ordered corundum materials have been primarily prepared as powders by solid-state<sup>12–19</sup> or wet-chemical synthesis<sup>20–22</sup> methods, and as thin films starting from mixed precursors<sup>23–26</sup>. As an

<sup>1</sup>Department of Materials Engineering, KU Leuven, Leuven, Belgium. <sup>2</sup>Department of Physics and Astronomy, KU Leuven, Leuven, Belgium. <sup>3</sup>Department of Electrical Engineering and Information Technology, ETH Zurich, Zurich, Switzerland. <sup>4</sup>Electron Microscopy for Materials Research (EMAT), University of Antwerp, Antwerp, Belgium. <sup>5</sup>Department of Electroceramics, Instituto de Cerámica y Vidrio-Consejo Superior de Investigaciones Científicas (ICV-CSIC), Madrid, Spain. <sup>6</sup>Department of Physics Education, Suncheon National University, Suncheon, Republic of Korea. <sup>7</sup>Department of Physics, Center for Extreme Quantum Matter and Functionality (CeQMF), Sungkyunkwan University, Suwon, Republic of Korea. <sup>8</sup>Imec, Leuven, Belgium. <sup>9</sup>These authors contributed equally: Claudio Bellani, Simon Mellaerts. ✉e-mail: [claudio.bellani@kuleuven.be](mailto:claudio.bellani@kuleuven.be); [maria.seo@kuleuven.be](mailto:maria.seo@kuleuven.be)

**Fig. 1 | Crystal structures of the ordered corundums.** Vanadium, chromium and oxygen atoms are represented in red, blue and gray, respectively. **a, d** Conventional and primitive corundum unit cell ( $R\bar{3}c$ ). The 6 atomic layers are highlighted as well as the ABC stacking. **b, e** conventional and primitive ilmenite unit cell ( $R\bar{3}$ ). **c, f** Conventional and primitive LNO unit cell ( $R\bar{3}c$ ).



alternative approach, we propose to leverage the atomic-layered growth via oxygen-assisted molecular beam epitaxy (MBE) to enable sub-unit cell engineering of corundum compounds and the stabilization of ordered corundum phases. This method provides several key advantages: access to a wider variety of A–B cation combinations, the opportunity to design tailor-made superlattice configurations, and the possibility of device integration.

In this work, we experimentally demonstrate the feasibility of constructing  $\text{Cr}_2\text{O}_3/\text{V}_2\text{O}_3$  superlattices with sub-unit-cell stacking. As the ultimate realization of this approach, a 1-monolayer (1 ML) superlattice is obtained, which, to the best of our knowledge, represents the first stabilization of the ilmenite phase of  $\text{CrVO}_3$ . The ordering of the alternating layers in this sub-unit cell regime has been directly evidenced by scanning transmission electron microscopy (STEM) combined with energy dispersive X-ray spectroscopy (EDX) and electron energy loss spectroscopy (EELS). Additionally, Raman spectroscopy has been employed to confirm symmetry lowering in these superlattices, as well as to verify the local ordering of the 1 ML  $\text{CrVO}_3$  superlattice into the  $R\bar{3}$  symmetry of the ilmenite structure. Finally, first-principles calculations predict that  $\text{CrVO}_3$  is a ferromagnetic insulator, consistent with previous studies<sup>9,27</sup>.

## Results and discussion

### Sub-unitcell engineered $\text{CrVO}_3$

$\text{CrVO}_3$  thin films were deposited by oxygen-assisted MBE on  $1 \times 1$  cm  $\text{Al}_2\text{O}_3$ -(0001) substrates at  $700^\circ\text{C}$  in ultra-high vacuum (chamber base pressure  $10^{-10}$  mbar). The molecular oxygen partial pressure was kept constant at  $2 \times 10^{-6}$  mbar during the deposition, as measured with a residual gas analyzer connected to the growth chamber. The negative in-plane lattice mismatch (compressive strain) of bulk  $\text{V}_2\text{O}_3$  and  $\text{Cr}_2\text{O}_3$  with the substrate is  $-4.2\%$  and  $-4.3\%$ , respectively. Therefore, a  $\text{Cr}_2\text{O}_3$  buffer layer was always deposited first on the  $\text{Al}_2\text{O}_3$  surface and followed by fully relaxed  $\text{CrVO}_3$  thin films<sup>28</sup>. The fluxes of evaporated Cr and V were calibrated with a quartz crystal microbalance at  $0.03 \text{ \AA/s}$ , while reflection high-energy electron diffraction (RHEED) was used to monitor in situ the layer-by-layer epitaxial growth of the crystalline oxide films. Figure 2a shows the RHEED pattern at the end of the growth of a  $\text{Cr}_2\text{O}_3$  buffer layer, confirming the epitaxial growth of the film. The RHEED intensity can be recorded as a function of time as represented in Fig. 2b: the measured periodic oscillations indicate the

layer-by-layer growth regime of the corundum thin film, and the period of about 40 s corresponds to the time required to form a complete single atomic layer at the calibrated growth rate. The RHEED oscillations, monitored during the growth of the  $\text{Cr}_2\text{O}_3$  buffer layer, were used to calibrate and fix the shutter-switching times for the entire growth of the superlattices. The superlattice structures were obtained by alternating the opening and closing of the Cr and V cell shutters according to the desired periodicity. The targeted structures consist of a sequence of the following repetition units:  $3\text{V} + 3\text{Cr}$  atomic layers,  $2\text{V} + 2\text{Cr}$  atomic layers, and  $1\text{V} + 1\text{Cr}$  atomic layers. Finally, a  $\text{CrVO}_3$  thin film with a 1:1 Cr:V stoichiometry was grown by co-deposition of Cr and V as a benchmark for the superlattice structures. Simple  $\text{Cr}_2\text{O}_3$  and  $\text{V}_2\text{O}_3$  epitaxial thin films on sapphire are used as a ref. 29.

The epitaxial growth of the buffer layer and of the superlattice thin film on the sapphire substrate is also confirmed by high-resolution X-ray diffraction (XRD)  $\omega-2\theta$  scans and high-angle annular dark-field STEM (HAADF-STEM) images in Fig. 2c, d. Additionally, the STEM-EELS spectra, measured across the entire thickness of the films, confirm the oxidation states of  $\text{Cr}^{3+}$  and  $\text{V}^{3+}$ . The  $\text{V}^{3+}$  oxidation state is confirmed by comparison of the V L-edge fine structure with both the  $\text{V}^{3+}$  reference spectrum plotted in Fig. 2e and the previously reported data by Lin et al.<sup>30</sup> and Hébert et al.<sup>31</sup>. Similarly, the  $\text{Cr}^{3+}$  oxidation state is verified using the  $\text{Cr}^{3+}$  reference spectrum shown in Fig. 2e and by applying the method proposed by Arévalo-López et al.<sup>32</sup>, in which the intensity ratio between the Cr  $L_3$  and  $L_2$ -edges is evaluated. The measured  $L_3/L_2$  ratio, ranging from 1.68 to 1.75 across the series of superlattice thin films, lies well within the expected interval for  $\text{Cr}^{3+}$ , thereby confirming its trivalent state. It is also noteworthy that the buffer layer exhibits the  $\text{Cr}^{3+}$  oxidation state. The fact that both Cr and V are stabilized in the 3+ oxidation state is particularly significant for two reasons. First, it rules out other common vanadium oxidation states, such as  $\text{V}^{4+}$  and  $\text{V}^{5+}$ <sup>33,34</sup>. Second, it marks a difference with existing  $\text{M}^{2+}\text{TiO}_3$  and  $\text{M}^{2+}\text{MnO}_3$  ilmenites, where two metals are arranged in a layered structure with 2+ and 4+ oxidation states, respectively<sup>12,15,18,35</sup>. Possibly, this can be attributed to the high stability of the  $\text{Cr}^{3+}$  cation<sup>36</sup> in comparison to  $\text{Cr}^{2+}$  and  $\text{Cr}^{4+}$ . As a result,  $\text{V}^{3+}$  seems to be stabilized when confined between  $\text{Cr}_2\text{O}_3$  layers. A logical extension would be to examine vanadium in combination with elements that are readily oxidized to  $\text{M}^{2+}$  and/or  $\text{M}^{4+}$  states.

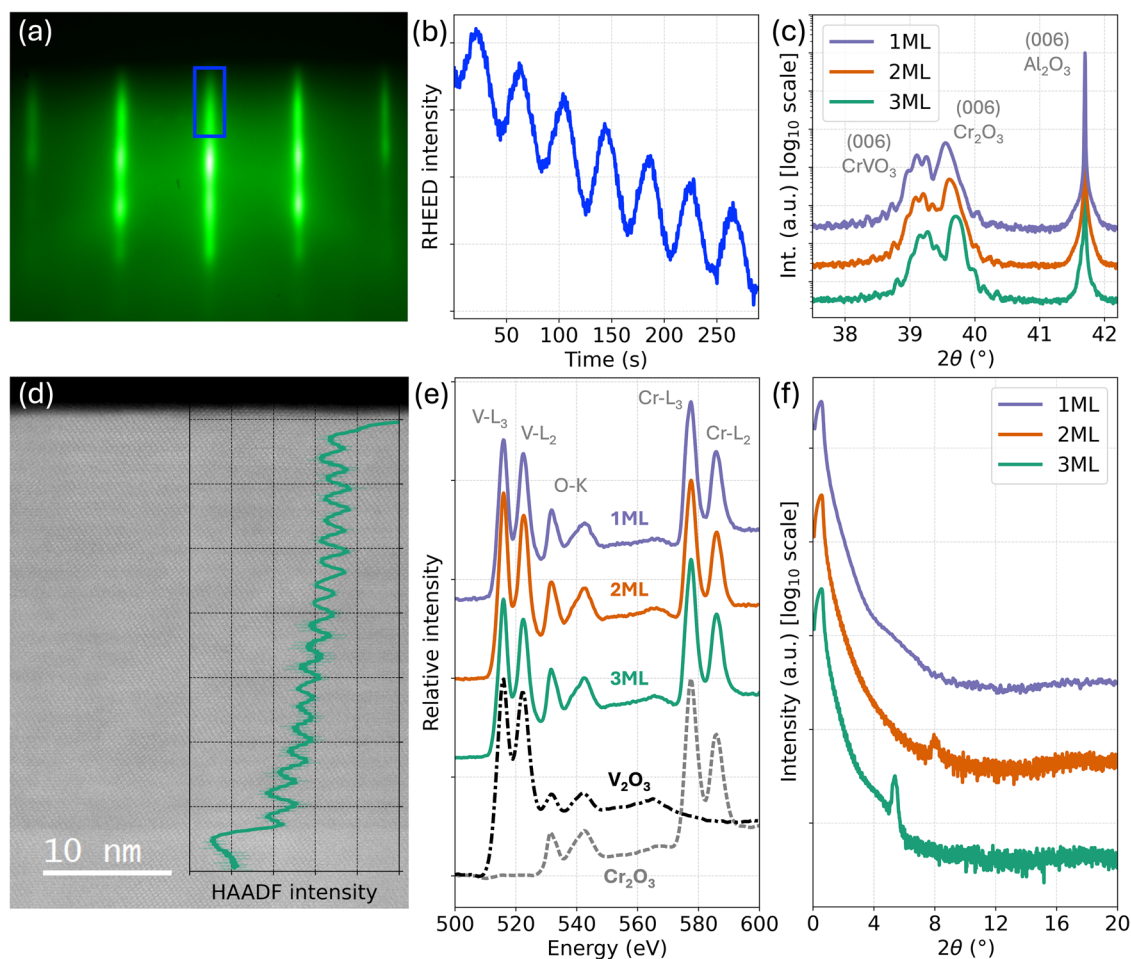


**Fig. 2 | Structural and EELS characterization of the superlattice thin films.** **a** RHEED pattern at the end of the growth of the  $\text{Cr}_2\text{O}_3$  buffer layer along the  $(\bar{1}210)$  direction. The blue rectangle indicates the region where the intensity has been recorded as a function of time. **b** RHEED intensity as a function of the deposition time. Each periodic oscillation corresponds to the completion of a single atomic layer. **c** HRXRD ( $\omega-2\theta$  scan) of the (006) peak of the corundum substrate, buffer layer and superlattice thin films. **d** Cross-sectional HAADF-STEM image of the 3 ML superlattice thin film along the  $(\bar{1}210)$  ZA. The interface with the  $\text{Cr}_2\text{O}_3$  buffer

layer is visible in the bottom part of the image. The inset plot represents the HAADF intensity along the  $z$ -direction and averaged across the width of the image. **e** STEM-EELS spectra near the V L<sub>3</sub>-edge, O K-edge and Cr L-edge measured over an area of several  $\text{nm}^2$  across the thickness of the thin films. The V L<sub>3</sub>-edge is used to align and normalize the intensity of the spectra. The  $\text{Cr}_2\text{O}_3$  and  $\text{V}_2\text{O}_3$  references were obtained from epitaxial thin films grown in the same MBE system. **f** XRR of the series of superlattice thin films.

Compared to the  $\text{Cr}_2\text{O}_3$  buffer layer, the superlattice thin film exhibits a distinct oscillation of the HAADF signal along the out-of-plane direction, attributed to the different atomic number ( $Z$ ) contrast between Cr and V. However, such contrast remains weak to effectively highlight and measure the periodicity of Cr–V superstructures with shorter periods (see Supplementary Fig. 1) because of the small  $Z$  difference.

In addition to the (006) and (0012) reflections that emerge from the ABC stacking in the corundum structure with space group  $R\bar{3}c$ , additional diffraction occurs in the 3 ML and 2 ML superlattices due to the artificially introduced periodicity. This results into higher-order reflections in the X-ray reflectivity (XRR) (see Fig. 2f) with a  $d$ -spacing of  $d_{3\text{ML}} = 16.5 \pm 0.4 \text{ \AA}$  and  $d_{2\text{ML}} = 11.0 \pm 0.4 \text{ \AA}$ , respectively. On the other hand, the removal of the glide reflection in the 1 ML superlattice with expected  $R\bar{3}$  space group symmetry would lead to a (0003) reflection in the diffractogram at  $2\theta \approx 19^\circ$  corresponding to  $d_{1\text{ML}} = 4.7 \text{ \AA}$ . However, such a reflection proved to be hard to detect, possibly due to the background and noise levels.

To confirm the measured periodicity and evaluate the interface quality of the periodical superstructures, STEM-EDX was performed. Figure 3 includes the elemental maps of all three superlattice thin films, as well as the corresponding line profile calculated along the out-of-plane direction. The Cr and V signals are periodic, with the Cr maxima matching with the V

minima. The period of the superlattice was calculated as the average distance between the Cr and V maxima, including the standard deviation to quantify its variability. In particular, the periods  $d_{3\text{ML}} = 16.3 \pm 0.9 \text{ \AA}$  and  $d_{2\text{ML}} = 11.0 \pm 1.2 \text{ \AA}$  are found to be in agreement with XRR. On the other hand, the 1 ML film presents a Cr–V periodicity only locally,  $d_{1\text{ML}} = 7.9 \pm 0.7 \text{ \AA}$ , explaining why the (0003) reflection was harder to detect in the X-ray diffractograms. Elemental mapping was also performed by STEM-EELS on the 2 ML and 1 ML samples. An absolute quantitative analysis is challenging due to the overlap of the V, Cr, and O edges (see Fig. 2e), but a relative estimate of the spatial distribution of Cr and V can be obtained by model-based quantification with the pyEELSmodel software<sup>37</sup>. The resulting spatial distributions of Cr and V along the out-of-plane direction in the 2 ML and 1 ML superlattices are plotted in Fig. 4a, b together with the HAADF signal. STEM-EELS confirms the ordering of the 2 ML superlattice (period  $d_{2\text{ML}} = 10.9 \pm 1.3 \text{ \AA}$ ) and the local cation ordering in the 1 ML thin film. However, the alignment of the Cr–V spatial distribution with the HAADF signal also highlights the errors in the 2Cr + 2V layers stacking; e.g., the Cr (or V) peak occasionally spans over 3 HAADF peaks corresponding to 3 atomic layers. The deviations from the designed Cr–V stacking periodicity can be explained by extrinsic factors, such as instabilities of the Cr and V evaporation fluxes during the deposition (Supplementary

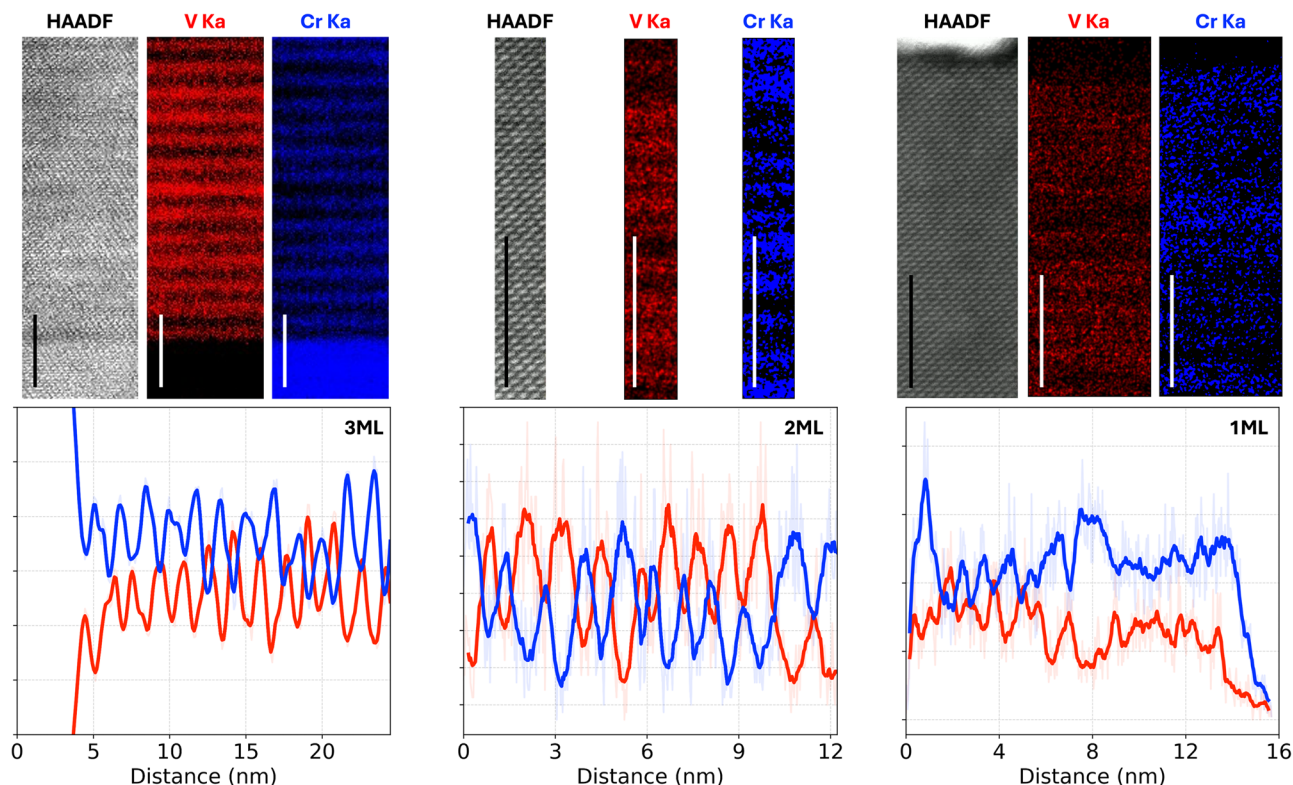


**Fig. 3 | Cross-sectional STEM-EDX chemical maps.** All data were acquired along the  $(\bar{1}210)$  zone axis, with the 3 ML, 2 ML, and 1 ML samples arranged from left to right. The top row contains the HAADF-STEM images with the corresponding STEM-EDX maps, and the bottom row shows the intensity profiles extracted from the maps. V and Cr distributions are mapped using the intensity of their respective  $K\alpha$  lines. The 3 ML sample map was processed with a Wiener filter, while the

corresponding intensity profile presents the unfiltered data. At the bottom, a portion of the  $\text{Cr}_2\text{O}_3$  buffer layer is also visible. To minimize the impact of surface steps on the chemical maps, the 2 ML and 1 ML samples were imaged from FIB lamellae thinner than 20 nm. Given the short interlayer distances of the 2 ML and 1 ML films, multi-frame imaging and spectroscopy data were acquired and aligned to correct for sample drift and scanning distortions. All scalebars represent 5 nm.

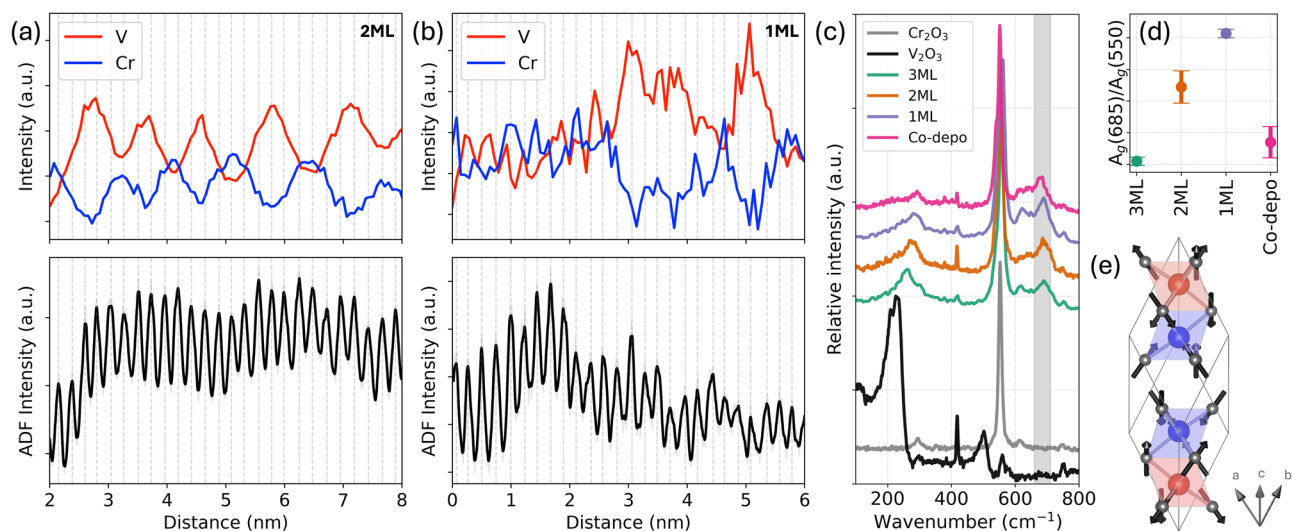


**Fig. 4 | STEM-EELS and Raman measurements confirm the periodicity of the superlattice thin films.** **a, b** HAADF-STEM and EELS profiles of the 2 ML and 1 ML superlattices. Vertical dashed lines are drawn matching the peaks in the HAADF signal, each corresponding to a single layer of cations. **c** Raman spectra of the superlattice thin films, compared to pure  $\text{V}_2\text{O}_3$ ,  $\text{Cr}_2\text{O}_3$ , and a co-deposited  $\text{CrVO}_3$  film. All the  $\text{V}_2\text{O}_3$  and  $\text{CrVO}_3$  films are grown on a  $\text{Cr}_2\text{O}_3$  buffer layer. As discussed

in the text, an additional  $A_g$  mode appears in the  $\text{CrVO}_3$  samples around  $685\text{ cm}^{-1}$ . The intensity of this mode is normalized to the intensity of the  $A_{1g}$  mode at  $550\text{ cm}^{-1}$  and is shown in **d**. The error bars represent the standard deviation of the signal noise. **e** Illustration of the Raman-activated  $A_g$  mode. The expansion (contraction) of the red (blue) octahedra is represented by the DFT-calculated eigenvectors (black arrows).

Figs. 2 and 3). However, intrinsic factors like interdiffusion cannot be ruled out, and they can impact the quality of the superlattice interfaces. Notably, antisite defects are expected to be structurally more favorable in  $ABO_3$  ordered corundum structures than perovskites because of the similar oxygen environments for A and B cations. Both sites have a six-fold oxygen coordination in a distorted octahedra, while in the perovskite lattice, A and B are surrounded by 12 and 6 O atoms, respectively. In the specific case of  $CrVO_3$ , we have shown that Cr and V have also the same valence state (Fig. 2e). In addition, Zhao et al.<sup>9</sup> calculated that the properties of ordered  $ABO_3$  corundums are not affected by the swap of A and B cations, suggesting a limited impact of antisite defects.

### Phonon spectroscopy to probe symmetry breaking

The introduced local symmetry breaking in the superlattices was evaluated by polarized Raman spectroscopy. As shown in Fig. 4, an additional band is detected around  $685\text{ cm}^{-1}$  in the  $CrVO_3$  samples in comparison to the sesquioxides  $Cr_2O_3$  and  $V_2O_5$ <sup>29,38</sup>. This is the highest observed frequency mode in the range  $100\text{--}1150\text{ cm}^{-1}$ , and its intensity increases as the superlattice period is reduced (Fig. 4d). A similar observation was made by Baraton et al.<sup>21</sup> for  $FeCrO_3$  powders obtained by co-precipitation, where they identified a new peak, the highest-frequency phonon mode around  $700\text{ cm}^{-1}$ , which was not observed in the parent oxides. As noted by the authors, the presence of the extra Raman band is a proof of cation ordering. The additional band is assigned to the inactive  $A_{2g}$  mode of  $A_2O_3$  corundum ( $R\bar{3}c$  space group), which becomes the Raman active  $A_g$  mode in the  $ABO_3$  ilmenite structure ( $R\bar{3}$  space group). Both modes correspond to the contraction and expansion of  $AO_6$  and  $BO_6$  octahedra in successive (0001) planes (Fig. 4e), resulting in the inactive  $A_{2g}$  if  $A=B$  in the parent  $A_2O_3$  corundum oxide, but Raman active ( $A_g$ ) if  $A\neq B$  in the  $ABO_3$  ilmenite structure. The same  $A_g$  assignment was made by Wang et al.<sup>39</sup> for  $MgTiO_3$ : 10 Raman modes are observed in the Raman spectrum as predicted by group theory and match the density functional theory (DFT) calculated frequencies for an ilmenite structure. The  $A_g$  mode is detected at  $715\text{ cm}^{-1}$ . Similarly, we calculated the frequencies of the Raman active modes in ilmenite  $CrVO_3$  (Supplementary Fig. 4): the calculated highest frequency mode is the  $A_g$  vibration described above, and we assign it to the highest observed frequency mode at  $685\text{ cm}^{-1}$ . To further confirm the  $A_g$  assignment, the Raman spectra were also collected as a function of the polarization angle (Supplementary Fig. 5). Consistent with the selection rules for the  $A_g$  mode, the band intensity exhibits a pronounced and gradual decrease when transitioning from parallel (VV)

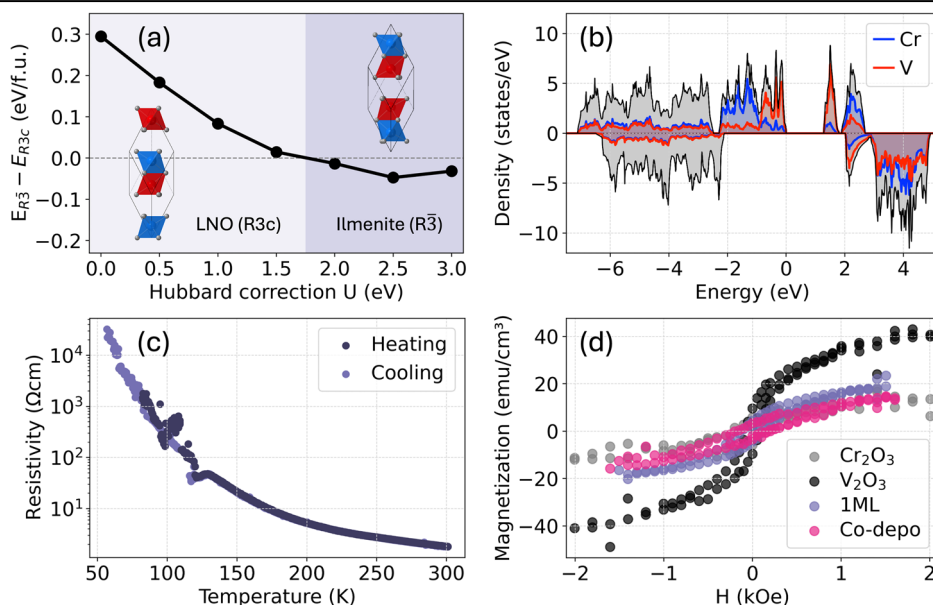
to cross (VH) polarization, providing a more robust evidence for the mode assignment.

Two additional  $A_{2g}$  modes are expected to be Raman active in the ilmenite  $R\bar{3}$  symmetry with their expected frequencies in the ranges  $\sim 186$  and  $\sim 395\text{ cm}^{-1}$  as predicted by DFT (Supplementary Table 1). The first overlaps with the  $A_{1g}$ -derived  $A_g$  mode, giving shape to an asymmetric peak (Supplementary Fig. 6). The second was not detected, either due to a smaller Raman polarizability or an overlap with the peaks of the buffer layer. Taking all the factors into account, we have demonstrated the presence of  $R\bar{3}$  symmetry features in the Raman spectra of all the superlattice thin films and the co-deposited  $CrVO_3$ . The last question to address is why such features are not observed solely in the 1 ML sample, which is designed to adopt the ilmenite structure with  $R\bar{3}$  symmetry. It is plausible to argue that the appearance of these features is caused by the symmetry breaking at the interfaces between the  $Cr_2O_3$  and  $V_2O_5$  layers. The same activation of a Raman inactive mode has already been observed in perovskite-based superlattices by Seong et al.<sup>40</sup> Such an interpretation would also be consistent with the increase in intensity of the  $A_g$  mode as the density of interfaces in the superstructures rises (i.e., with the decreasing period of the superlattice), as shown in Fig. 4d. In the broader context, it indicates that the cations in the 1 ML sample exhibit at least local ordering, as previously demonstrated by STEM-EDX and STEM-EELS. Furthermore, it suggests the presence of a self-ordering mechanism in the co-deposited sample, though less effective than the periodic opening and closing of the shutters, as evidenced by the weaker  $A_g$  peak. This result should not be surprising for two reasons. First, the structural stability of ilmenite  $CrVO_3$ , as calculated in this work, aligns with previous literature findings<sup>9,27</sup>. Second, ilmenite structures have already been successfully synthesized using methods, such as solid-state reactions and co-precipitation, which do not impose superstructure periodicity and must therefore rely on a form of self-ordering<sup>12,15,18-21,41,42</sup>.

### Ferromagnetic insulating ilmenite

By DFT calculations, the relative stability of both the non-centrosymmetric ilmenite and the polar LNO structure were evaluated as a function of Hubbard correction ( $U$ ), as shown in Fig. 5a. It can be anticipated that a Hubbard value of 3 eV is considered an appropriate approximation for  $CrVO_3$ , based on prior works of  $V_2O_5$  and  $Cr_2O_3$ <sup>43,44</sup>. Henceforth, it is inferred that the ilmenite structure is energetically favored. Subsequently, the electronic properties were evaluated, as depicted in Fig. 5a. An insulating behavior is observed with an estimated energy gap of 1.28 eV. Finally, the

**Fig. 5 | Functional properties of  $CrVO_3$  with  $R\bar{3}$  ilmenite structure.** **a** Energy comparison of the ilmenite ( $R\bar{3}$ ) and the LNO ( $R\bar{3}c$ ) structures as a function of the Hubbard correction  $U$  for  $CrVO_3$ . The background color and the crystal models indicate what structure is the most stable in the two regions of the phase diagram. **b** The Cr and V contributions to the partial DOS of ilmenite  $CrVO_3$ . **c** Resistivity of the  $CrVO_3$  1 ML superlattice thin film. **d** Magnetization of  $CrVO_3$ ,  $V_2O_5$  and  $Cr_2O_3$  thin films as a function of the external magnetic field  $H$  at 10 K and with  $H$  parallel to the in-plane lattice direction.



magnetic ordering and main magnetic interactions were evaluated by considering five different short-period spin arrangements (see Supplementary Fig. 7). By an energy comparison, it is shown that FM ordering is energetically favored above 2 eV, with magnetic moments  $M_V = 2.02 \mu_B$  and  $M_{Cr} = 3.07 \mu_B$ , in excellent agreement with prior work<sup>9</sup>. Although a strong exchange interaction of 52.2 meV exists along the short Cr–V dimer, the relative energy stability of FM is only 14 meV/f.u. compared to the lowest AF state (at  $U = 3$  eV). This might suggest a relatively weak FM ordering.

Following up on the DFT calculations, a preliminary investigation into the functional properties of the 1 ML superlattice thin film was performed. The resistivity measurement as a function of temperature shows a clear insulating behavior as the sample is cooled down to 50 K from room temperature (Fig. 5c). The thin film is confirmed to be insulating by UV–VIS spectroscopy (see Supplementary Fig. 8), but a reliable estimate of the band gap proved to be challenging due to the overlap with the optical features of the  $\text{Cr}_2\text{O}_3$  buffer layer, i.e. its 3.1 eV band gap and crystal field excitations of  $\text{Cr}^{3+}$  ions at 2.1 and 2.6 eV<sup>45</sup>. At last, the magnetic properties of the  $\text{CrVO}_3$  1 ML superlattice were assessed and compared to  $\text{Cr}_2\text{O}_3$ ,  $\text{V}_2\text{O}_3$  and co-deposited  $\text{CrVO}_3$  thin films. The measured magnetization  $M$  as a function of the magnetic field  $H$  is shown in the Fig. 5d. All the samples present a weak ferromagnetic response along both field directions (in and out-of-plane) and at both probed temperatures (300 and 10 K). The largest remnant magnetization is observed in the  $\text{V}_2\text{O}_3$  thin film, in all the four combinations of  $H$  direction and sample temperature (see Fig. 5d and Supplementary Fig. 9); this is in contrast with the expected paramagnetic behavior of  $\text{V}_2\text{O}_3$ <sup>46</sup>. This weak ferromagnetism could arise from extrinsic effects such as superparamagnetic clusters or glassy dynamics, which in  $\text{V}_2\text{O}_3$  thin films may arise from magnetic impurities or defects associated with the epitaxial growth on sapphire. A similar ambiguity exists for ilmenite  $\text{CrVO}_3$ ; however, the  $\text{CrVO}_3$  thin films exhibit a larger coercive field ( $H_c \sim 85$  Oe at 300 K and  $H_c \sim 130$  Oe at 10 K for the 1 ML superlattice). Additional measurements are required to establish whether the increased coercive field reflects the presence of intrinsic long-range magnetic order.

## Conclusions

The results presented in this work demonstrate an approach to the synthesis of ordered corundum oxides, leveraging the atomic layer-by-layer growth of epitaxial thin films.  $\text{CrVO}_3$  superlattice thin films have been grown by oxygen-assisted MBE, progressively reducing the thickness of the alternating  $\text{Cr}_2\text{O}_3$  and  $\text{V}_2\text{O}_3$  layers. Specifically, the  $\text{M}_2\text{O}_3$  units consist of 3, 2 or 1 layer of cations, i.e., one half, one third or one sixth of the conventional corundum unit cell height. A detailed structural characterization showed how the superlattices can be controlled at the atomic scale, although the induced Cr–V alternation may be in competition with interdiffusion at the 1 ML limit at the growth temperature of 700 °C. Moreover, antisite defects are expected to be structurally more favorable if compared to perovskites due to the similar sixfold O-coordination of the Cr and V sites. Despite the challenges involved, this approach towards the synthesis of ordered corundum structures opens a promising path for the growth of artificial functional oxide thin films, whose properties depend on the layering configuration in the corundum lattice and the chosen pair of cations. First-principles calculations have shown the potential of 1 ML limit, i.e., ilmenite and LNO structures, while the properties of sub-unit cell superlattices need to be explored in detail in future studies.

## Methods

The XRD  $\omega$ – $2\theta$  scan and XRR experiments were conducted with a Rigaku TF-XRD-300 system, equipped with a dual rotating Cu anode and a HyPix-3000 detector. The system was operated with a  $\text{Ge}220 \times 2$  monochromator in the incident optics for the XRD measurements.

Raman spectra were acquired at room temperature using a 100× objective with a numerical aperture of 0.95. An output laser power of 40 mW was used to avoid the overheating effects and possible damage to the sample. Raman spectra were collected in the spectral range 65–1160  $\text{cm}^{-1}$

using an 1800  $\text{g mm}^{-1}$  grating. Under optimal conditions, the spectral resolution is 0.02  $\text{cm}^{-1}$ . In turn, the vibrational properties were also evaluated as a function of polarization angle. Here, the polarization analyzer detector is adjusted from 0° (parallel polarization, VV) to 90° (cross polarization, VH) against the incident polarization. Raw Raman data were processed with Witec Project Plus software (version 2.08).

Cross-sectional lamellae were prepared by focused ion beam (FIB) for STEM imaging and elemental mapping using DualBeam Nova 600 NanoLab, then analyzed with a cold-FEG JEOL ARM200F microscope operated at 200 kV, equipped with a STEM-Cs corrector, a Centurio EDX spectrometer and a Gatan Tridiem electron energy loss spectrometer. EELS spectra were collected with a collection semi-angle of 16.7 mrad and a beam current of 120 pA. For the 1 ML and 2 ML samples, thinner lamellas were prepared on a Dual beam FIB/SEM Helios Nanolab 650. A more detailed analysis was performed on a Themis Z microscope, which is an aberration-corrected STEM, Thermo Fisher Scientific Titan3 60–300 operated at an acceleration voltage of 200 kV, equipped with a high-brightness field-emission electron source (X-FEG) and an electron monochromator excited to 1.4, providing an energy resolution better than 200 meV while keeping a spatial resolution of 1 Å. EDX and EELS were acquired simultaneously using a collection semi-angle of 56 mrad and a beam current of 50 pA. Multiple EELS data were acquired on a prototype Iliad EELS Spectrometer with Zebra EELS detector developed by Thermo Fisher with a dispersion of 0.05 eV/pixel<sup>47</sup>. Core-loss EELS data analysis was performed using model-based quantification with the pyEELSmodel software<sup>37</sup>. The core-loss data were aligned using the zero-loss peak and spatially binned to improve the signal-to-noise ratio of the spectra and facilitate the fitting procedure. Relative estimates of spatial variations of Cr and V can be extracted using model-based fitting reliably. The model consisted of three parts. First, a convexity constrained linear background<sup>48</sup>. Second, core-loss edges using the cross sections for O, V and Cr<sup>49</sup>. Third, a component considering multiple scattering based on the low loss signal. For EDX elemental mapping of the 2 ML and 1 ML superlattices, multi-frame EDX data was acquired, using the simultaneously acquired HAADF signal.

The resistivity of the 1 ML superlattice thin film was measured in the Van der Pauw configuration with a Keithley 4200-SCS parameter analyzer between 50 and 300 K. UV–vis absorbance spectra were acquired using a Tecan Infinite 200 PRO microplate reader. A magnetic property measurement system based on a superconducting quantum interference device magnetometer was used to characterize the magnetic properties of a selection of thin films. The relatively strong diamagnetic signal due to the substrate was fitted in the high fields regions (5 kOe <  $|H|$  < 30 kOe) and subsequently subtracted from the measured magnetization (see Supplementary Figs. 10 and 11).

All DFT calculations were carried out using the Vienna ab initio simulation package<sup>50</sup>. The interactions between electrons and ions were treated using the projector augmented-wave method<sup>51</sup>, and the electronic wave functions were expanded with a plane-wave cutoff energy of 600 eV. The PBEsol exchange-correlation functional<sup>52</sup> was employed throughout, while the localized nature of the  $3d$  electrons of the cations was treated by a Hubbard correction  $U$  within the rotationally invariant approach proposed by Dudarev et al.<sup>53</sup>. Structural relaxations were performed with a force convergence criterion of 0.005 eV/Å, and the Brillouin zone was sampled using a  $\Gamma$ -centered  $12 \times 12 \times 12$   $k$ -point mesh. For the electronic and magnetic calculations, a dense  $24 \times 24 \times 24$  mesh was used with an energy convergence criterion of  $10^{-6}$  eV. The phonon dispersions were evaluated by density functional perturbation theory and with the use of the PHONOPY package<sup>54</sup>.

## Data availability

The data that support the findings of this study are available from the corresponding author, Jin Won Seo (maria.seo@kuleuven.be), upon reasonable request.

Received: 23 July 2025; Accepted: 31 December 2025;

Published online: 19 January 2026

## References

1. Goldschmidt, V. M. Die Gesetze der Krystallochemie. *Naturwissenschaften* **14**, 477–485 (1926).
2. Glazer, A. M. The classification of tilted octahedra in perovskites. *Acta Crystallogr. Sect. B* **28**, 3384–3392 (1972).
3. Chen, P. et al. Energetics of oxygen-octahedra rotations in perovskite oxides from first principles. *Phys. Rev. B* **97**, 024113 (2018).
4. Xiang, H. J., Guennou, M., Íñiguez, J., Kreisel, J. & Bellaiche, L. Rules and mechanisms governing octahedral tilts in perovskites under pressure. *Phys. Rev. B* **96**, 054102 (2017).
5. Catalano, S. et al. Rare-earth nickelates  $RNiO_3$ : thin films and heterostructures. *Rep. Prog. Phys.* **81**, 046501 (2018).
6. Nordlander, J., Anderson, M. A., Brooks, C. M., Holtz, M. E. & Mundy, J. A. Epitaxy of hexagonal  $ABO_3$  quantum materials. *Appl. Phys. Rev.* **9**, 031309 (2022).
7. Imada, M., Fujimori, A. & Tokura, Y. Metal-insulator transitions. *Rev. Mod. Phys.* **70**, 1039–1263 (1998).
8. Cai, G.-H., Greenblatt, M. & Li, M.-R. Polar magnets in double corundum oxides. *Chem. Mater.* **29**, 5447–5457 (2017).
9. Zhao, H. J., Bellaiche, L. & Íñiguez, J. First-principles screening of  $ABO_3$  oxides with two magnetic sublattices. *Phys. Rev. Mater.* **3**, 064406 (2019).
10. Zhou, W. X. & Ariando, A. Review on ferroelectric/polar metals. *Jpn. J. Appl. Phys.* **59**, SI0802 (2020).
11. Bhowal, S. & Spaldin, N. A. Polar metals: principles and prospects. *Annu. Rev. Mater. Res.* **53**, 53–79 (2023).
12. Chamberland, B., Sleight, A. & Weiher, J. Preparation and characterization of  $MgMnO_3$  and  $ZnMnO_3$ . *J. Solid State Chem.* **1**, 512–514 (1970).
13. Syono, Y., Akimoto, S.-I. & Endoh, Y. High pressure synthesis of ilmenite and perovskite type  $MnVO_3$  and their magnetic properties. *J. Phys. Chem. Solids* **32**, 243–249 (1971).
14. Sheikh, A. & Irvine, J. Phase formation and electronic transport properties in the corundum ( $Ti_2O_3$ )-ilmenite ( $MgTiO_3$ ) system. *J. Solid State Chem.* **103**, 30–37 (1993).
15. Sohn, J.-H. et al. Microwave dielectric characteristics of ilmenite-type titanates with high  $q$  values. *Jpn. J. Appl. Phys.* **33**, 5466 (1994).
16. Aimi, A. et al. High-pressure synthesis and correlation between structure, magnetic, and dielectric properties in  $LiNbO_3$ -type  $MnMO_3$  ( $M = Ti, Sn$ ). *Inorg. Chem.* **50**, 6392–6398 (2011).
17. Li, M.-R. et al. A polar corundum oxide displaying weak ferromagnetism at room temperature. *J. Am. Chem. Soc.* **134**, 3737–3747 (2012).
18. Akaogi, M. et al. High-pressure phase behaviors of  $ZnTiO_3$ : ilmenite–perovskite transition, decomposition of perovskite into constituent oxides, and perovskite–lithium niobate transition. *Phys. Chem. Miner.* **42**, 421–429 (2015).
19. Rodrigues, J. E. et al. Unveiling the infrared complex dielectric function of ilmenite  $CdTiO_3$ . *J. Alloy. Compd.* **813**, 152136 (2020).
20. Swoboda, T., Toole, R. & Vaughan, J. New magnetic compounds of the ilmenite-type structure. *J. Phys. Chem. Solids* **5**, 293–298 (1958).
21. Baraton, M., Busca, G., Prieto, M., Ricchiardi, G. & Escribano, V. S. On the vibrational spectra and structure of  $FeCrO_3$  and of the ilmenite-type compounds  $CoTiO_3$  and  $NiTiO_3$ . *J. Solid State Chem.* **112**, 9–14 (1994).
22. Meena, D., Bhatnagar, M. & Singh, B. Synthesis, characterization and gas sensing properties of the rhombohedral ilmenite  $CdSnO_3$  nanoparticles. *Phys. B Condens. Matter* **578**, 411848 (2020).
23. Popova, E. et al. Systematic investigation of the growth and structural properties of  $FeTiO_3 \pm \delta$  epitaxial thin films. *J. Appl. Phys.* **103**, 093909 (2008).
24. Varga, T. et al. Epitaxial growth of  $NiTiO_3$  with a distorted ilmenite structure. *Thin Solid Films* **520**, 5534–5541 (2012).
25. Varga, T., Droubay, T. C., Kovarik, L., Hu, D. & Chambers, S. A. Controlling the structure and ferroic properties of strained epitaxial  $NiTiO_3$  thin films on sapphire by post-deposition annealing. *Thin Solid Films* **662**, 47–53 (2018).
26. Miura, K., Fujiwara, K. & Tsukazaki, A. Growth control of corundum-derivative  $MnSnO_3$  thin films by pulsed-laser deposition. *AIP Adv.* **9**, 035210 (2019).
27. Le, H.-L., Goniakowski, J. & Noguera, C. Properties of mixed transition metal oxides:  $MM' O_3$  in corundum-type structures ( $M, M' = Al, Ti, V, Cr, \text{ and } Fe$ ). *Phys. Rev. Mater.* **2**, 085001 (2018).
28. Dillemans, L. et al. Evidence of the metal-insulator transition in ultrathin unstrained  $V_2O_3$  thin films. *Appl. Phys. Lett.* **104**, 071902 (2014).
29. Hsu, W.-F. et al. Raman spectroscopy and phonon dynamics in strained  $V_2O_3$ . *Phys. Rev. Mater.* **7**, 074606 (2023).
30. Lin, X., Wang, Y., Dravid, V., Michalakos, P. & Kung, M. Valence states and hybridization in vanadium oxide systems investigated by transmission electron-energy-loss spectroscopy. *Phys. Rev. B* **47**, 3477 (1993).
31. Hébert, C. et al. Oxygen k-edge in vanadium oxides: simulations and experiments. *Eur. Phys. J. B Condens. Matter Complex Syst.* **28**, 407–414 (2002).
32. Arevalo-Lopez, A. M. & Alario-Franco, M. A. Reliable method for determining the oxidation state in chromium oxides. *Inorg. Chem.* **48**, 11843–11846 (2009).
33. Kosuge, K. The phase diagram and phase transition of the  $V_2O_3$ - $V_2O_5$ , system. *J. Phys. Chem. Solids* **28**, 1613–1621 (1967).
34. Katzke, H., Tolédano, P. & Depmeier, W. Theory of morphotropic transformations in vanadium oxides. *Phys. Rev. B* **68**, 024109 (2003).
35. Ishikawa, Y. & Sawada, S. The study on substances having the ilmenite structure I. Physical properties of synthesized  $FeTiO_3$  and  $NiTiO_3$  ceramics. *J. Phys. Soc. Jpn.* **11**, 496–501 (1956).
36. White, W. B. & Roy, R. The system chromium-oxygen at high oxygen pressures. in *Chromium: its Physicochemical Behavior and Petrologic Significance* 803–817 (Elsevier, 1976).
37. Verbeeck, J. Pyeelsmodel <https://github.com/joverbee/pyEELSMODEL> (2024).
38. Mellaerts, S. et al. Confinement-induced isosymmetric metal-insulator transition in ultrathin epitaxial  $V_2O_3$  films. *ACS Appl. Mater. Interfaces* **16**, 23476–23483 (2024).
39. Wang, C.-H., Jing, X.-P., Feng, W. & Lu, J. Assignment of Raman-active vibrational modes of  $MgTiO_3$ . *J. Appl. Phys.* **104**, 034112 (2008).
40. Jeong, S. G., Seo, A. & Choi, W. S. Atomistic engineering of phonons in functional oxide heterostructures. *Adv. Sci.* **9**, 2103403 (2022).
41. Cloud, W. Crystal structure and ferrimagnetism in  $NiMnO_3$  and  $CoMnO_3$ . *Phys. Rev.* **111**, 1046–1049 (1958).
42. Matthias, B. & Remeika, J. Ferroelectricity in the ilmenite structure. *Phys. Rev.* **76**, 1886 (1949).
43. Grieger, D. & Fabrizio, M. Low-temperature magnetic ordering and structural distortions in vanadium sesquioxide  $V_2O_3$ . *Phys. Rev. B* **92**, 075121 (2015).
44. Shi, S., Wysocki, A. L. & Belashchenko, K. D. Magnetism of chromia from first-principles calculations. *Phys. Rev. B* **79**, 104404 (2009).
45. Sala, V. G. et al. Resonant optical control of the structural distortions that drive ultrafast demagnetization in  $Cr_2O_3$ . *Phys. Rev. B* **94**, 014430 (2016).
46. McWhan, D., Menth, A., Remeika, J., Brinkman, W. & Rice, T. Metal-insulator transitions in pure and doped  $V_2O_3$ . *Phys. Rev. B* **7**, 1920 (1973).
47. Jannis, D. et al. Multi element ELNES mapping of compounds. In *Proc. BIO Web of Conferences*, Vol. 129, 06010 (EDP Sciences, 2024).

48. Van den Broek, W., Jannis, D. & Verbeeck, J. Convexity constraints on linear background models for electron energy-loss spectra. *Ultramicroscopy* **254**, 113830 (2023).
  49. Zhang, Z. et al. Relativistic EELS scattering cross-sections for microanalysis based on Dirac solutions. *Ultramicroscopy* **269**, 114083 (2025).
  50. Kresse, G. & Furthmüller, J. Efficient iterative schemes for ab initio total-energy calculations using a plane-wave basis set. *Phys. Rev. B* **54**, 11169–11186 (1996).
  51. Kresse, G. & Joubert, D. From ultrasoft pseudopotentials to the projector augmented-wave method. *Phys. Rev. B* **59**, 1758–1775 (1999).
  52. Perdew, J. P. et al. Restoring the density-gradient expansion for exchange in solids and surfaces. *Phys. Rev. Lett.* **100**, 136406 (2008).
  53. Dudarev, S. L., Botton, G. A., Savrasov, S. Y., Humphreys, C. J. & Sutton, A. P. Electron-energy-loss spectra and the structural stability of nickel oxide: an LSDA+U study. *Phys. Rev. B* **57**, 1505–1509 (1998).
  54. Togo, A. & Tanaka, I. First principles phonon calculations in materials science. *Scr. Mater.* **108**, 1–5 (2015).
- by S.M., W.-F.H., and C.B. DFT calculations were performed by S.M. and M.H. C.B. wrote the manuscript with input from all authors. All authors reviewed and approved the manuscript.

### Competing interests

The authors declare no competing interests.

### Additional information

**Supplementary information** The online version contains supplementary material available at <https://doi.org/10.1038/s43246-025-01069-7>.

**Correspondence** and requests for materials should be addressed to Claudio Bellani or Jin Won Seo.

**Peer review information** *Communications Materials* thanks Honggyu Kim and the other anonymous reviewer(s) for their contribution to the peer review of this work.

**Reprints and permissions information** is available at <http://www.nature.com/reprints>

**Publisher's note** Springer Nature remains neutral with regard to jurisdictional claims in published maps and institutional affiliations.

**Open Access** This article is licensed under a Creative Commons Attribution-NonCommercial-NoDerivatives 4.0 International License, which permits any non-commercial use, sharing, distribution and reproduction in any medium or format, as long as you give appropriate credit to the original author(s) and the source, provide a link to the Creative Commons licence, and indicate if you modified the licensed material. You do not have permission under this licence to share adapted material derived from this article or parts of it. The images or other third party material in this article are included in the article's Creative Commons licence, unless indicated otherwise in a credit line to the material. If material is not included in the article's Creative Commons licence and your intended use is not permitted by statutory regulation or exceeds the permitted use, you will need to obtain permission directly from the copyright holder. To view a copy of this licence, visit <http://creativecommons.org/licenses/by-nc-nd/4.0/>.

© The Author(s) 2026

### Acknowledgements

This work was financially supported by the KUL C14/21/083, by the FWO infrastructure projects I000920N and AKUL/13/19, and the FWO IRI project I002123N. N.G., Z.Z., and J.V. acknowledge the funding from the European Union's Horizon 2020 research and innovation program under grant agreement no. 823717-ESTEEM3. A.A. acknowledges the IMPRESS project that has received funding from the HORIZON EUROPE framework program for research and innovation under grant agreement no. 101094299. J.L.-S. acknowledges the financial support from grant PID2023-151036OA-I00 funded by MICIU/AEI/10.13039/501100011033 and by ERDF, EU, and from grant RYC2022-035912-I funded by MCIU/AEI/10.13039/501100011033 and by the European Social Fund Plus (ESF+). This work was supported by National Research Foundation of Korea (NRF) grants funded by the Korean government (MSIT) RS-2023-00220471 and RS-2023-00240326.

### Author contributions

J.W.S., J.-P.L., and S.M. conceived and supervised the project. Sample growth was performed by S.M., C.B., and K.S. Characterization measurements were carried out as follows: X-ray characterization by S.M., W.-F.H., and C.B.; TEM characterization by C.B., A.A., Z.Z., N.G., and J.V.; UV-vis spectroscopy by A.B.; Raman spectroscopy by J.L.-S. and A.C.; magnetic measurements by S.-G.J. and T.P.; and resistivity measurements